Structural phase transitions in yttrium up to 183 GPa

E. J. Pace, S. E. Finnegan, C. V. Storm, M. Stevenson, and M. I. McMahon
SUPA, School of Physics and Astronomy, and Centre for Science at Extreme Conditions, The University of Edinburgh, Peter Guthrie Tait Road, Edinburgh EH9 3FD, United Kingdom

S. G. MacLeod
Atomic Weapons Establishment, Aldermaston, Reading RG7 4PR, United Kingdom and SUPA, School of Physics and Astronomy, and Centre for Science at Extreme Conditions, The University of Edinburgh, Peter Guthrie Tait Road, Edinburgh EH9 3FD, United Kingdom

E. Plekhanov, N. Bonini, and C. Weber
Theory and Simulation of Condensed Matter (TSCM), Department of Physics, King's College London, The Strand, London WC2R 2LS, United Kingdom

(Received 27 July 2020; accepted 1 September 2020; published 16 September 2020)

Angle-dispersive x-ray powder diffraction experiments have been performed on yttrium metal up to 183 GPa. We find that the recently discovered $oF16$ structure observed in the high-Z trivalent lanthanides is also adopted by yttrium above 106 GPa, pressures where it has a superconducting temperature of ∼20 K. We have also refined both tetragonal and rhombohedral structures against the diffraction data from the preceding "distorted-fcc" phase and we are unable to state categorically which of these is the true structure of this phase. Finally, analysis of yttrium's equation of state reveals a marked change in the compressibility upon adoption of the $oF16$ structure, after which the compression is that of a "regular" metal. Electronic structure calculations of $oF16$-Y confirm its stability over $oF8$ structure seen in Nd and Sm, and provide insight into the nature of the shift of orbital character from s to d under compression.

DOI: 10.1103/PhysRevB.102.094104

I. INTRODUCTION

The trivalent transition metals yttrium (Y) and scandium (Sc) are considered members of the rare-earth elements, along with the lanthanide series (La to Lu). The unique structural and material properties exhibited by the rare-earth elements at extreme pressures has incentivized a great number of experimental and theoretical studies [1–7]. The regular trivalent lanthanides (La to Lu, excluding Ce, Eu and Yb) each exhibit a common phase transition sequence on compression, the structures of which differ only in the stacking arrangement of their close-packed atomic layers: hcp (space group $P6_3/mmc$, $hP2$ in the Pearson notation) → α-Sm type ($R\bar{3}m$, $hR9$) → double-hcp ($P6_3/mmc$, $hP4$) → face-centred cubic ($Fm\bar{3}m$, $cF4$) → distorted-$cF4$ ($R\bar{3}m$, $hR24$) [1,8,9]. As the reverse sequence of structures ($hP4$–$hR9$–$hP2$) is adopted by the same elements at ambient conditions as one traverses them with increasing atomic number (Z), it was initially thought to arise from changes in the occupancy of the f-band with Z or with pressure. However, Y, which has no f electrons, was later shown to exhibit the same transition sequence on compression [10,11], and the subsequent reassessment of the structural changes found that they arise from an increase in the d-band occupancy, as a result of $s \rightarrow d$ electron transfer [9]. Y has thus historically been used as a benchmark for comparing the electronic character of the structural transitions in the rare-earth metals [10–13].

None of the phase transitions listed above results in a measurable volume change [6]. However, upon further compression, the distorted-$cF4$ phase transforms to a "collapsed" phase accompanied by a discontinuity in the atomic volume [3,5,6]. This transition occurs at ∼95 GPa in Y with a volume change of −2.6% [13]. For the last 20 years, the structure of the collapsed phases was generally perceived to be either orthorhombic ($Cmcm$, $oC4$) in Ce, Pr, Nd and Sm, or monoclinic ($C2/m$, $mC4$) in Ce, Nd, Sm, Tb, Gd, Dy, Ho, Er, Tm, and Y (see Ref. [6], and references cited therein). The fits of the $mC4$ structure to the reported diffraction data were typically poor, except in the case of Ce [14,15], and we have recently shown that the true structure of the collapsed phase in Tb, Gd, Dy, Ho, Er, and Tm is orthorhombic, space group $Fddd$ with 16 atoms per unit cell ($oF16$) [7], while in Nd and Sm it is also orthorhombic with space group $Fddd$, but with eight atoms per unit cell ($oF8$) [16]. The $oF8$ structure was previously found in the actinides Cf, Am, and Cm at high pressure [17–19] and the $oF16$ and $oF8$ structures, along with the $hP3$ structure observed in Nd, Sm, and Yb [20,21], form a new family of structures which differ only in the stacking sequence of their quasi-close-packed layers [7].

Remarkably, while the *oF*16 structure had not previously been observed experimentally in any element, although it has recently been confirmed as the stable phase of Ho above 103 GPa [22], both it and the *hP*3 structure were calculated to be the stable phase(s) of Y above 97 GPa [12,23,24], pressures at which Y has a remarkably high superconducting transition temperature (T_c) of 19.5 K at 115 GPa [25]. It is then a reasonable assumption that the superconducting phase adopts one of these two structures, as both *oF*16 and *hP*3 are estimated to have a T_c in the range of 16–19 K at 97 GPa [23,26]. Furthermore, electronic structure calculations have found that shifts of the *d* electron states to low-energy levels, and a significant decrease in the density of states (DOS) at the Fermi level, contribute to the stabilities of both the *oF*16 and *hP*3 structures [23]. In addition, the accumulation of electrons into interstitial sites in both structures was also reported to play an important role in their stability [23].

The diffraction patterns from the *mC*4 and *oF*16 structures are somewhat similar, which led to the incorrect assignment of the former to the collapsed phases of the high-*Z* trivalent lanthanides [7]. The previous determination of the structure of Y above 100 GPa as being *mC*4 [13] then suggests that the structure is more likely to be *oF*16 rather than *hP*3, which has a different and much simpler diffraction pattern [20]. In order to determine the true structure of Y above 100 GPa, we have made diffraction studies to 183 GPa using x-ray powder diffraction and synchrotron radiation. We find that Y does indeed adopt the *oF*16 structure above 95 GPa, in agreement with computational studies [23,24]. Our result confirms that the high-pressure structural behavior of Y and the trivalent lanthanides is indeed very similar, but different to that of the other rare-earth element Sc [27].

The high quality of our diffraction data also enabled us to address another long-standing issue with the rare-earth series, that is, the crystal structure of the distorted-*cF*4 phase (d-*cF*4). Although the most widely accepted structure, including in Y, is *hR*24 (space group $R\bar{3}m$) [28,29], other possibilities have been suggested in order to explain peak splittings which are forbidden by the rhombohedral symmetry of this structure, for example in Dy [30]. In Y, recent *ab initio* density functional theory (DFT) calculations have suggested tetragonal or triclinic distortions of *hR*24 as being the true structure of the d-*cF*4 phase [31], and we have tested these new models against our diffraction data.

II. EXPERIMENT

We conducted synchrotron x-ray diffraction experiments on four separate Y samples, attaining a maximum pressure of 183 GPa at 300 K. Diamond anvil cells (DACs) equipped with diamond culets ranging in diameter from 80 to 300 μm were prepared with tungsten (W) gaskets and the sample chamber was filled with Y powder (99.9% purity, Sigma Aldrich) under a dry Ar atmosphere (<1 ppm O_2 and <1 ppm H_2O) to prevent oxidation. A Cu sphere ~5 μm in diameter was loaded into three of the DACs as a pressure calibrant, while a small ruby sphere was used as a calibrant in the fourth. Angle-dispersive diffraction data were collected at the high pressure beamlines P2.02 at PETRA-III in Hamburg, at beamline I15 at the Diamond Light Source (DLS), and at beamline 9.5HP at the now-closed Synchrotron Radiation Source (SRS) at Daresbury Laboratory in the UK. Monochromatic x-rays of wavelength 0.34439 Å (PETRA-III), 0.42454 Å (DLS), and 0.44379 Å (SRS) were focused down to a FWHM of 2 μm (PETRA), 20 μm (DLS), and 50 μm (SRS). Diffraction data were recorded on a Perkin-Elmer area detector (PETRA-III) and a MAR345 image-plate detector (DLS and SRS). In one run at PETRA-III the detector was initially placed ~400 mm from the sample, and later increased to ~600 mm to improve the low-angle peak resolution, while in other runs at PETRA-III the detector was maintained at ~400 mm. At DLS and SRS the detectors were maintained at ~300 mm from the sample. The exact sample-detector distance and the detector tilts were determined using diffraction standards (LaB_6, CeO_2 and Si). The sample pressures were derived from the published Cu equation of state (EoS) [32] and standard ruby fluorescence calibration data [33,34]. The 2D diffraction images were integrated to 1D profiles using DIOPTAS [35], and these were analysed using Rietveld and Le Bail profile fitting [36,37], and least-squares [38] to individual peak positions.

III. RESULTS AND DISCUSSION

At ambient pressure, Y crystallizes in the *hP*2 structure and this produced sharp, well-defined diffraction peaks (Fig. 1) and atomic volumes in excellent agreement with previous compression studies [10,11]. The transition from *hP*2 to the *hR*9 structure has been described previously as sluggish, starting at 13 GPa and becoming complete at 16 GPa [13]. We observed the transition to start at 14 and 16 GPa in two different samples, and observed the *hR*9 phase only as a minority component in mixed-phase samples along with either *hP*2 (at lower pressures) or *hP*4 (at higher pressures). Indeed, the similarities of the *hP*2, *hR*9, *hP*4 and *cF*4 structures, which differ only in the stacking of their close-packed atomic layers—e.g., AB in *hP*2 and ABACACBCB in *hR*9—resulted in significant overlap of diffraction peaks from the different phases, and sluggish transitions that produced mostly mixed-phase diffraction patterns.

These effects were perhaps exacerbated by the absence of any pressure transmitting medium (PTM) in our samples, which typically increases non-hydrostaticity. However, we note that neither Vohra *et al.* [10] nor Samudrala *et al.* [13] reported the use of a PTM in their previous studies of Y. Using the 2 μm diameter x-ray beam at PETRA-III we used 'grid-scans' to map out the pressure gradients within the samples at a number of pressures. These scans revealed not only pressure variations of 4 GPa within the sample volume at 89 GPa, and 7 GPa at 125 GPa, but also revealed that these variations resulted in different phase mixtures being present at different locations within the samples. We obtained accurate compressibility data, and reduced the effects of pressure gradients and mixed-phase samples, by ensuring that our diffraction patterns contained diffraction peaks from both the Y sample and Cu pressure marker, and utilizing the small x-ray beam size available at PETRA-III to ensure that the pressure gradients within the sampled volume were minimal. Preliminary experiments using the larger (20 μm) x-ray beam at the DLS resulted in both more complex mixed-phase diffraction patterns, and

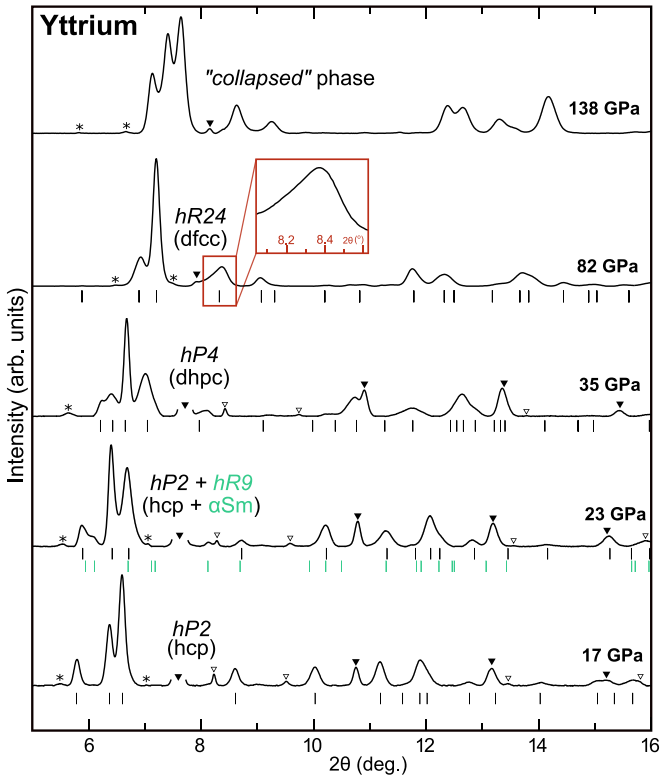

FIG. 1. Background-subtracted angle-dispersive diffraction profiles from Y collected on compression showing the diffraction patterns obtained from each of the different phases. For the four profiles collected below 95 GPa, the reflection positions predicted by the different phases ($hP2$, $hP2 + hR9$, $hP4$ and $hR24$, respectively) are indicated by vertical bars below each profile. The profile collected at 138 GPa is from the "collapsed" phase. The ▼ symbols identify peaks from the W gasket, ▽ denotes peaks from the Cu calibrant and asterisks identify weak peaks from a sample impurity. The $(2\bar{2}4)$ peak in the $hR24$ profile at 82 GPa is enlarged in the inset to highlight the asymmetric shape that may indicate it is a closely spaced doublet—something that is forbidden by the rhombohedral symmetry of the $hR24$ structure.

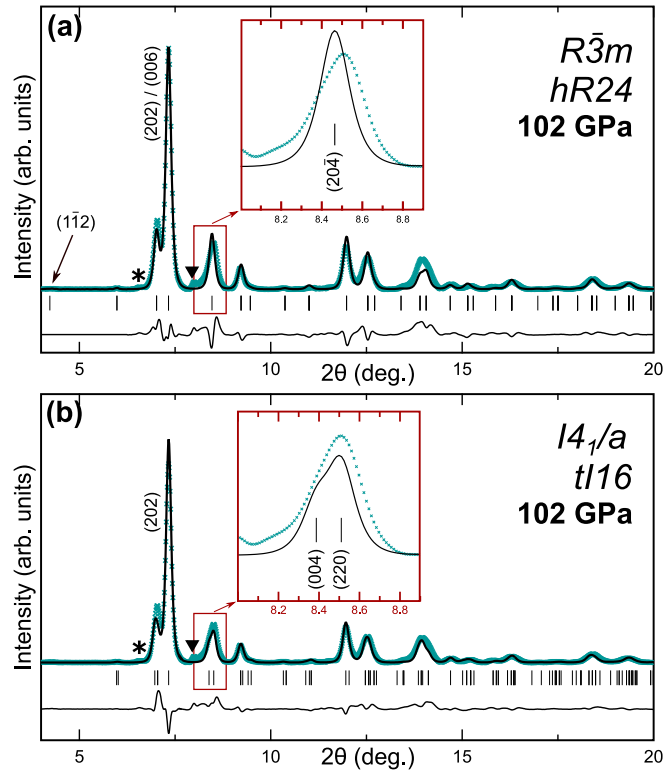

FIG. 2. Rietveld refinements of the (a) $hR24$ and (b) $tI16$ structures to a diffraction profile of Y obtained at 102 GPa, showing the observed (cyan crosses) and calculated (black line) diffraction patterns. The calculated reflection positions (vertical bars), principal Miller indices, and difference profiles (lower lines) are shown. The ▼ symbols identify a weak peak from the W gasket, and the asterisks identify a weak peaks from a sample impurity. The same diffraction peak is highlighted in both profiles illustrating how it is fitted as a singlet in $hR24$ and a doublet in $tI16$. The $(1\bar{1}2)$ peak, which is predicted by the $hR24$ structure at 4.2° but not by the $tI16$ structure, is highlighted in (a) The refined structural parameters are (a) $a = 5.554(1)$ Å, $c = 13.604$ Å, atoms at (0.521(1),−0.521(1),0.243(1)) and (0,0,0.269(1)) and (b) $a = 5.524(1)$ Å, $c = 7.926(2)$ Å, atoms at (0.528(1),0.219(1),0.890(1)).

discrepancies in the compressibility data due to the pressure gradients within the much larger (∼100×) sampled volume.

While complex mixed-phase samples were often observed below 52 GPa, only single-phase diffraction patterns from the d-$cF4$ phase were observed above that pressure. If the d-$cF4$ phase of Y has the $hR24$ structure, then the $cF4 \rightarrow hR24$ transition produces two changes to the diffraction pattern. Firstly, the distortion from cubic to rhombohedral symmetry results in the peaks of the cubic $cF4$ structure splitting at the transition. Importantly, the (200) peak in the $cF4$ pattern remains a singlet in $hR24$ [where it indexes as the $(20\bar{4})$—see inset to Fig. 2(a)], while the most intense (111) $cF4$ peak splits into a doublet [which index as the (202) and (006) peaks]. Secondly, additional diffraction peaks appear at the transition as a result of the enlarged unit cell of the $hR24$ structure and the movements of the atoms at the transition to lower-symmetry sites.

Studies of single-phase d-$cF4$ profiles from Y between 52 and 102 GPa using the $hR24$ structure revealed that the (202)/(006) doublet remains unresolved at all pressures, and the same is true for the higher-angle (404)/(00,12) doublet, which would have a larger splitting than the (202)/(006). The overlap of the peaks in these doublets implies that the c/a ratio is indistinguishable from $\sqrt{6}$ at all pressures. This is in marked contrast to the behavior seen in the $hR24$ phases of Pr [39], and Sm [40], where the (202)/(006) and (404)/(00,12) peaks are clearly resolved into doublets, and the c/a ratio increases rapidly with pressure. Importantly, the (200) peak in the $cF4$ phase (which indexes as the $(20\bar{4})$ in the $hR24$ structure) shows some evidence of being a closely spaced doublet in the d-$cF4$ diffraction profiles in Y, as highlighted in the 82 GPa profile in Fig. 1. A similar doublet, which is forbidden by the $hR24$ structure, was seen in diffraction profiles from the d-$cF4$ phase of Dy, and this was used by Shen *et al.* to argue that d-$cF4$ phase of Dy has orthorhombic rather than rhombohedral symmetry [30].

The computational study of Y by Chen *et al.* suggested that the d-$cF4$ phase of Y has the $hR24$ structure [12], and

this was confirmed experimentally soon afterwards by Samudrala *et al.* [13]. However, more recently, Ishikawa *et al.* [31] have reported that two distortions of the *hR*24 structure, with tetragonal and triclinic symmetry, also have low enthalpies over the relevant pressure range, with the former having the slightly lower enthalpy between 40 and 80 GPa. Analysis of the atomic coordinates of the tetragonal structure listed by Ishikawa *et al.* [31] reveal it to be body-centred rather than primitive, and to have spacegroup $I4_1/a$ ($tI16$) with atoms on the 16*f* sites at (0.5295,0.2327,0.8918). This structure becomes $cF4$ when $c = \sqrt{2}a = 2a_{\mathrm{FCC}}$ and the atoms are at (0.5,0.25,0.875). A key feature of the $tI16$ structure is that the (111) reflection in $cF4$ remains a singlet in $tI16$, while the (200) reflection becomes a doublet. In contrast, if the d-$cF4$ phase of Y were to adopt the *oS*8 structure, first proposed by Porsch and Holzapfel [41] and reported to be the structure of the d-$cF4$ phase of Dy [30], then both the (111) *and* the (200) peaks would become doublets. In the triclinic structure suggested by Ishikawa *et al.* [31], the (111) and the (200) peaks would split into 4 and 3 peaks, respectively. The $tI16$ structure therefore provides a high-symmetry, few-parameter solution to the structure of the d-$cF4$ phase when the (111) peak of $cF4$ remains a singlet while the (200) becomes a doublet.

As highlighted in Fig. 1, there is some evidence of the (200) peak of the $cF4$ becoming split in the d-$cF4$ phase of Y, although this is evident only as an asymmetry on the low-angle side of the peak. A Rietveld fit of the $tI16$ structure to a profile obtained at 102 GPa [see Fig. 2(b)] is excellent, and the refined structure is shown in Fig. 3(a). The relationship of the $tI16$ structure to that of $cF4$ is illustrated in Fig. 3(b).

However, despite the excellent fit of the $tI16$ structure, there are no clear features (apart from the possible doublet at 8.5°) not also accounted for in a fit using the *hR*24 structure with $c/a = \sqrt{6}$ [see Fig. 2(a)]. While higher resolution profiles would make distinguishing the two structures straightforward, since they have different symmetry and predict a multitude of different peak splittings, our current data are unable to decide definitively between the two structural models. The *hR*24 structure also predicts an additional low-angle peak at ~4.2° [the $(1\bar{1}2)$] not accounted for by $tI16$, but it is predicted to be extremely weak, and was not observed previously in either Pr or Sm [39,40]. We are thus unable to determine the structure of the d-$cF4$ phase of Y definitively, despite the quality of our diffraction data, and to obtain its compressibility we have refined it as having the *hR*24 structure with the constraint $c/a = \sqrt{6}$ [see Fig. 2(a)].

We observe the transition to the "collapsed" phase of Y at 106 GPa (Fig. 5), which is much closer to the most recently predicted transition pressure of 109 GPa [24], than the 95 GPa reported by Samudrala *et al.* [13]. The onset of the transition is clearly evident from the splitting of the (202)/(006) doublet (of *hR*24), see Fig. 1, and is complete by 117 GPa. A Rietveld refinement of the $Fddd$ ($oF16$) structure to the diffraction profile obtained at 138 GPa is shown in Fig. 4, and the fit is excellent. The $oF16$ structure comprises eight quasi-close-packed layers with a b/c axial ratio of $\sqrt{2.9}$—ideal packing would give an axial ratio of $\sqrt{3}$. In $oF16$ the atoms of each layer are located above the saddle point between two

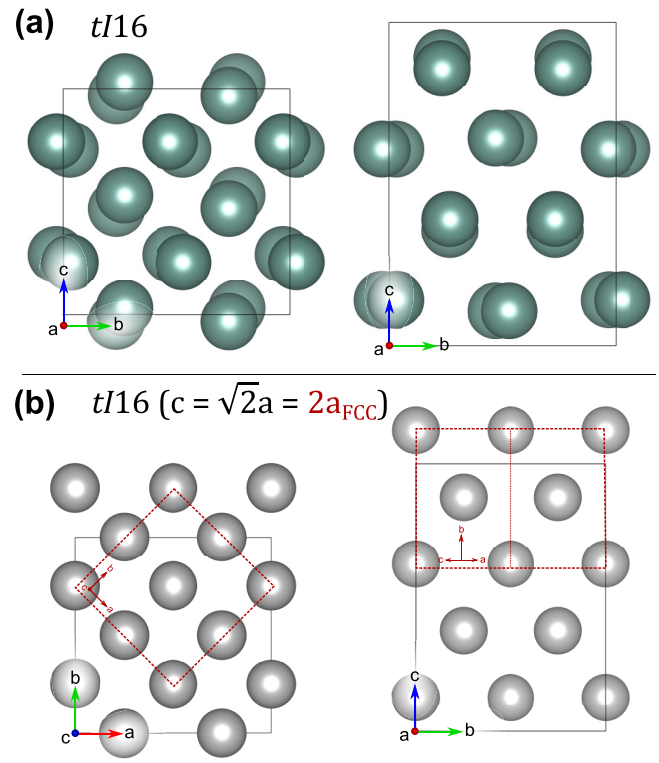

FIG. 3. (a) The $tI16$ structure of Y at 102 GPa with $a = 5.524(1)$ Å and $c = 7.926(2)$ Å, $c/a \sim \sqrt{2.06}$, and atoms located on the 16*f* site at (0.528(1), 0.219(1), 0.890(1)). (b) The $tI16$ structure with $c = \sqrt{2}a = 2a_{\mathrm{FCC}}$, which reproduces the $cF4$ structure when the atoms are at (0.5,0.25,0.875). The cubic FCC unit cell highlighted by dotted lines.

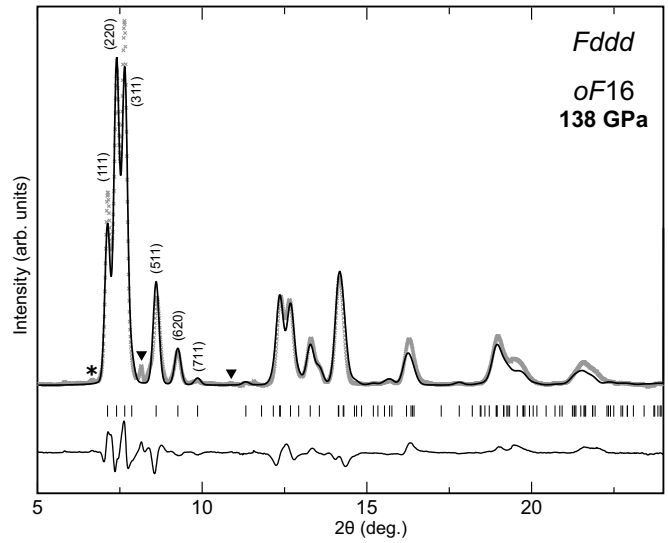

FIG. 4. Rietveld refinement of the $oF16$ structure to a diffraction profile from Y at 138 GPa, showing the observed (cyan crosses) and calculated (line) diffraction patterns, the calculated reflection positions, and the difference profile. The ▼ symbols identify peaks from the W gasket, and the asterisk identifies a weak peak from a sample impurity. Space group $Fddd$ with Y atoms on the 16*e* (x,0,0) Wyckoff sites with $x = 3/16$ (fixed), $a = 16.911(3)$ Å, $b = 4.656(1)$ Å, and $c = 2.728(1)$ Å.

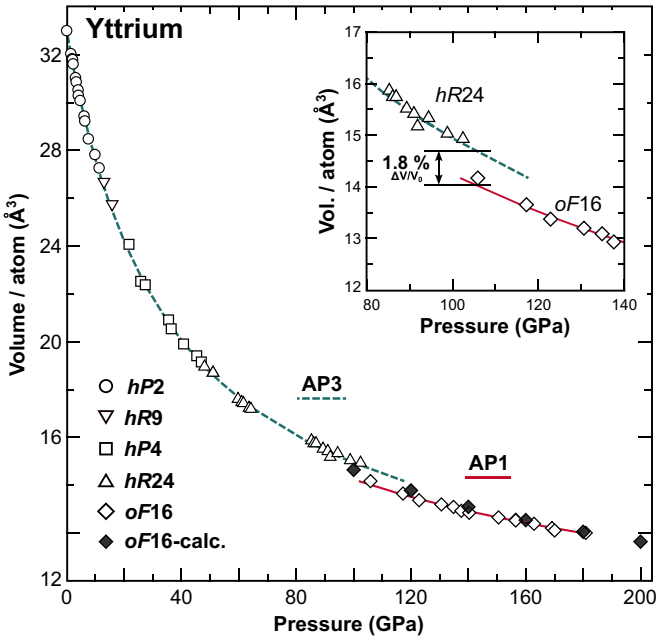

FIG. 5. The compressibility of Y to 183 GPa, shown as the volume per atom versus pressure (GPa). Open symbols refer to experimental data while the filled diamonds are atomic volumes of the $oF16$ phase determined from our DFT calculations. The inset shows an enlarged view of the region near the $hR24 \rightarrow oF16$ transition, highlighting the -1.8% volume change ($\Delta V/V_0$). The dashed line through the data points below 100 GPa is the best-fitting AP3 equation of state (EoS) with $V_0 = 33.0177$ Å^3 (fixed), $K_0 = 47.3(6)$ GPa, $K' = 1.90(13)$, and $K'' = -0.017(6)$. The solid line through the data from the $oF16$ phase is a best-fitting AP1 EoS with $K_0 = 11.56(4)$ GPa $K' = 6.02(2)$ and V_0 is fixed at 32.42 Å^3/atom, the value for $oF16$-Y at ambient pressure and 0 K as determined from our DFT calculations.

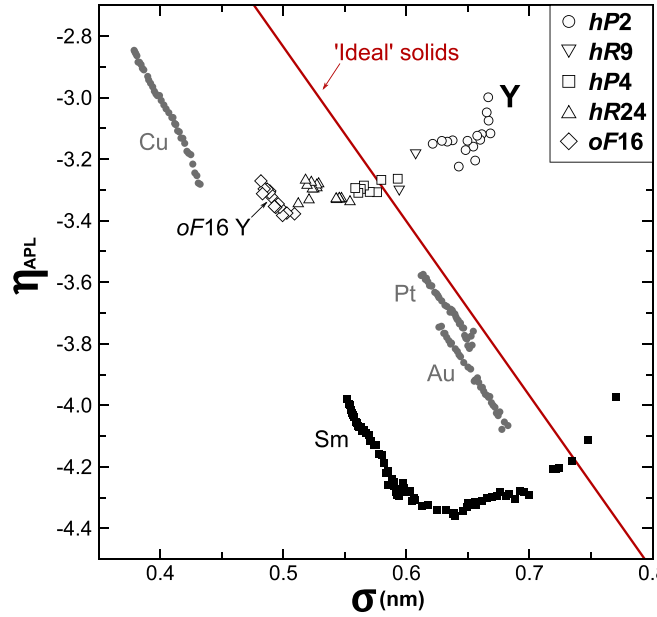

FIG. 6. Linearization of compressibility of Y in the form of an $\eta_{\rm APL} - \sigma$ plot, where $\sigma = \sigma_0 x$, $x = (V/V_0)^{1/3}$ and σ_0 is the Thomas-Fermi radius $(3ZV_0/4\pi)^{\frac{1}{3}}$. The data from the different phases of Y are plotted using different symbols, alongside the same plot for Sm (irregular compressibility, black filled squares) and the "regular" compressibilities of Cu, Au and Pt (grey filled circles), as determined from the compression data of Dewaele *et al.* [42] for comparison. The red line labeled "ideal solids" has the gradient $\bar{\eta} = -5.67$ nm^{-1}, and is the average gradient expected for all elements with regular compression [43,44].

atoms in the preceding layer, resulting in ten-fold coordination $(6 + 2 + 2)$, whereas in close-packed $hP2$, $hP4$, $hR9$ and $cF4$, each atom is located at the central point between the three closest atoms in the previous layer, resulting in twelve-fold coordination $(6 + 3 + 3)$. The $oF16$ structure has an eight-layer stacking sequence - ABCADCBD - twice that of the four-layer ABCD repeat sequence of the isosymmetric $oF8$ structure observed in Sm, Nd, Am, Cm, and Cf [7,16–19].

The compressibility of Y up to 183 GPa is shown in Fig. 5. A volume change (ΔV/V$_0$) of -1.8% (see inset to Fig. 5) is observed at the transition to the "collapsed" phase, much closer to typical volume changes observed in the equivalent transition amongst the other rare-earth elements than the discontinuity of -2.6% reported by Samudrala *et al.* when using the $C2/m$ structure to analyze the collapsed phase [13]. The theoretical work of Chen *et al.* reported that the stability of the $oF16$ structure in Y arises from the shift in the d-electron energy levels, which results in the transfer of s electrons to the d band [23]. Such changes in the electronic structure can result in changes in compressibility, which are most easily visualizing by linearizing the compressibility curve, enabling one to distinguish anomalies arising from changes within the electronic structure from the standard compressive behavior expected of a "normal" metal [44].

If one fits the compression data using the second order (AP2) form of the adapted polynomial of order L (APL) EoS [43,44]:

$$P = 3K_0 \frac{(1-x)}{x^5} \exp(c_0(1-x)) \left(1 + x \sum_{k=2}^{L} c_k (1-x)^{k-1}\right), \tag{1}$$

where K_0 is the zero pressure bulk modulus, K' is its pressure derivative, $x = (V/V_0)^{1/3}$, $c_0 = -\ln(3K_0/p_{\rm FG})$, $c_2 = (3/2)(K' - 3) - c_0$, $p_{\rm FG} = a_{\rm FG}(Z/V_0)^{5/3}$ is the Fermi-gas pressure, Z is the atomic number, and $a_{\rm FG} = [(3\pi^2)/5](\hbar^2/m_e) = 0.02337$ GPa nm^5 is a constant, then the compression data can be linearized in a so-called $\eta_{\rm APL} - x$ plot:

$$\eta_{\rm APL}(x) = \ln\left(\frac{px^5}{p_{\rm FG}}\right) - \ln(1-x), \tag{2}$$

where $x = (V/V_0)^{1/3}$, the Fermi-gas pressure $p_{\rm FG} = a_{\rm FG}(Z/V_0)^{5/3}$, and $a_{\rm FG} = 0.02337$ GPa nm^5.

To realize differences in compression data of different materials with respect to "ideal" behavior, it is most convenient to use an APL linearization not with respect to x but rather to $\sigma = \sigma_0 x$, with σ_0 being the Thomas-Fermi radius $(3ZV_0/4\pi)^{\frac{1}{3}}$, because this scaling brings out common trends more clearly [44].

The linearized $\eta_{\rm APL} - \sigma$ data for Y is shown in Fig. 6, along with the similarly linearized data we have recently reported for Sm [16] and the data for the "regular" metals Cu,

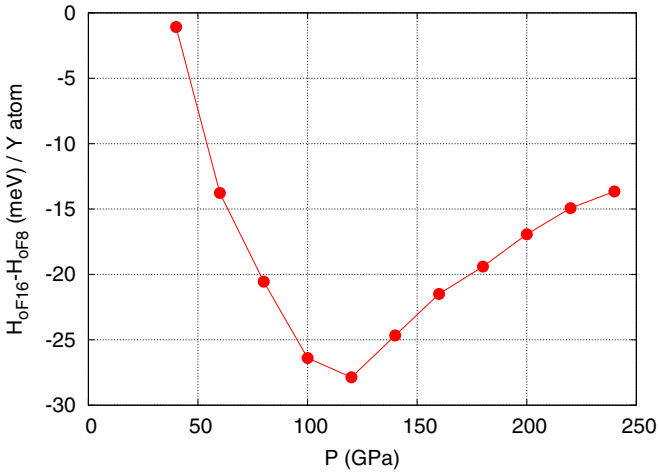

FIG. 7. The enthalpy difference between *oF*16-Y and the *oF*8-Y as a function of pressure, as calculated within DFT. The difference is normalized per Y atom and exhibits a minimum around $P = 120$ GPa.

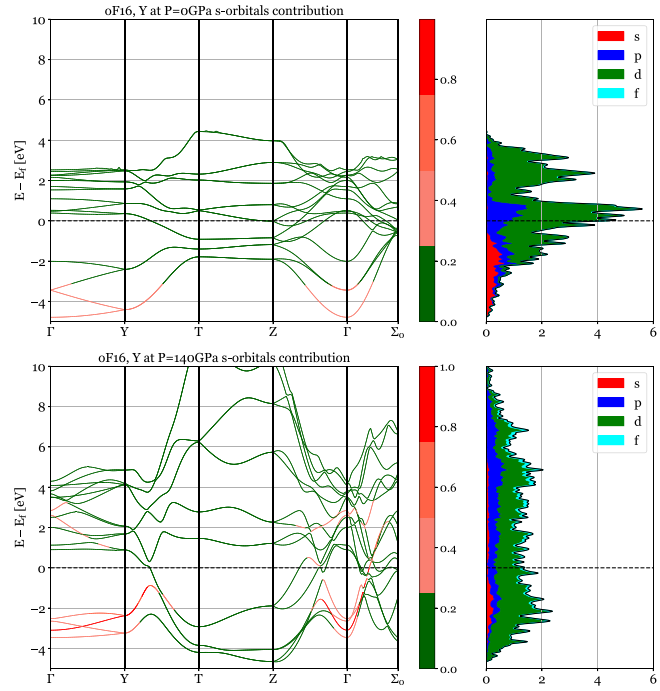

FIG. 8. Band structure (BS) and density of states (DOS) for *oF*16-Y at ambient pressure (top) and at 140 GPa (bottom). The color code of the BS plot reflects the predominant orbital character: either *s* (red) or *d* (green). The color code of the "stacked" DOS plots corresponds to the orbital character: 'red for *s*-orbital, blue for *p*-orbital, 'green for *d*-orbital, and cyan for *f*-orbital. These plots were made by using the PYPROCAR package [45].

Au, and Pt [42]. In such a plot, materials undergoing "normal" compressive behavior will show linear or quasi-linear behavior with an average "ideal" gradient of -5.67 nm^{-1} and with the correct theoretical limit of $\eta_{\mathrm{APL}}(0) = 0$. This behavior is clearly demonstrated by Cu, Au, and Pt in Fig. 6, while Sm provides an excellent example of a material whose compressibility is initially "irregular" as a result of *s*-*d* electron transfer, but which becomes "regular" after it transforms to the *oF*8 structure. Although the data from the lower-pressure phases of Y exhibit some scatter amongst the linearized η_{APL} values, a general positive gradient can be identified, similar to that shown by Sm. However, on entering the *oF*16 phase, there is a clear shift to linear behavior with a negative gradient very similar to that found in Sm, Cu, Au, and Pt. Although the pressure range over which we have compression data for *oF*16-Y (80 GPa) is somewhat smaller than the 100+ GPa pressure range over which we have compression data for *oF*8-Sm, the linearized data in Fig. 6 suggest that *oF*16-Y, like *oF*8-Sm, is a metal with 'regular' compressibility.

The positive gradient exhibited by the lower-pressure phases of Y in Fig. 6 suggests that the compression curve shown in Fig. 5 would not be well fitted by an AP2 EoS. This was indeed the case, and we found that a 3rd-order AP3 form was required, as shown in Fig. 5. However, the regular compression of the *oF*16 phase means that it could be well fitted using a 1st-order AP1 EoS (Fig. 5).

IV. ELECTRONIC STRUCTURE CALCULATIONS

As said, the transition to regular compressive behavior in the collapsed *oF*16 phase may arise from a discrete change in the electronic structure of Y. Indeed the recent electronic band structure calculations of Li *et al.* for *oF*16-Y exhibited metallic features, with the majority of the DOS at the Fermi level collected in the 4*d*-band, transferred from the 4*s* band [24]. This supports prior models predicting high critical Coulomb pseudopotentials for *oF*16, and it would be interesting to obtain a linearized plot (similar to Fig. 6) from compression data collected below the predicted superconducting transition pressure, to observe if such treatment of standard compressibility data could provide additional insight into other material behaviours affected by its electronic structure.

To gain further insight, we have performed extensive DFT calculations of the *oF*16 and *oF*8 phases of Y. Structural optimization of bulk Y in the *oF*8 and *oF*16 phases was accomplished by using the DFT calculations with the help of the VASP [46] package using the Perdew-Burke-Ernzerhof functional [47]. The *k*-point sampling was performed using a Monkhorst-Pack mesh of $8\times16\times2$ for the *oF*8 and $8\times12\times2$ for the *oF*16 structures in the tetragonal unit cell, respectively, and a Gaussian smearing of 0.1eV. During the DFT structural optimization, the convergence on internal forces and stress tensor of 0.01 eV/Å was reached, and the energy cutoff was set to 500 eV. Scalar relativistic spin-orbit coupling was taken into account within the Koelling-Harmon approximation [48].

Our zero-temperature DFT calculations for Y demonstrate that the *oF*16 phase is lower in enthalpy than the *oF*8 phase at all pressures between 40 and 240 GPa, as shown in Fig. 7, with the maximum enthalpy gain being reached near 120 GPa. The agreement of our DFT zero-temperature volume calculations for *oF*16-Y as a function of pressure with the room-temperature experimental data is also very good, as can be seen from Fig. 5. The absence of the imaginary phonon modes in the *oF*16 phase was previously established in the work of Chen *et al.* [23].

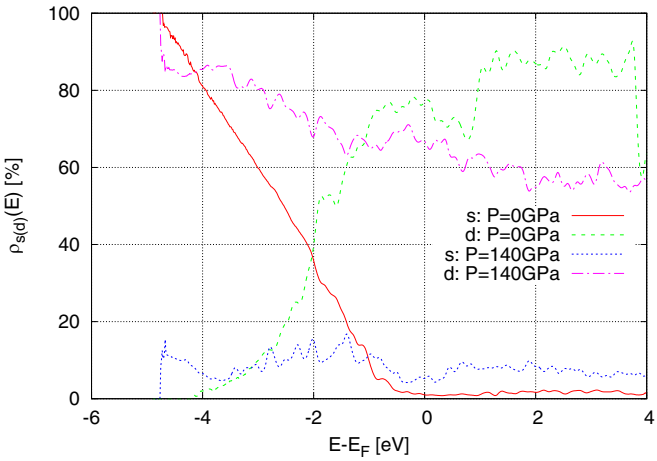

FIG. 9. Relative contribution to the total DOS of the s and d states at $P = 0$ GPa (solid red line: s states, dashed green line: d states) and at $P = 140$ GPa (dotted blue line: s states, dashed-dotted magenta line: d states).

The qualitative change of the valence electrons' orbital character in the $oF16$-$Fddd$ can be best seen from the combined band structure and density-of-states plots at ambient and at high pressures, as shown in Fig. 8. It can be seen that the major contribution to the band structure in the energy range of $[-5 : 10]$ eV comes from the s and d states, while the main effect of the pressure on Y is to increase dramatically the bandwidth of the d states. Indeed, by applying pressure from 0 to 140 GPa, the d state's bandwidth increases by a factor of two. At the same time, the s states, located around 4 eV below the Fermi energy, are slightly raised by around 1eV and are strongly hybridized with the d states, as a result of applied pressure.

In order to underline the difference in contribution of the s and d states to the total DOS at high and low pressure, in Fig. 9, we plot the quantities

$$\rho_s(E) = \frac{D_s(E)}{D_{\text{tot}}(E)}, \quad \rho_d(E) = \frac{D_d(E)}{D_{\text{tot}}(E)}, \tag{3}$$

where $D_s(E)$, $D_d(E)$, and $D_{\text{tot}}(E)$ are the partial s, partial d and the total DOS, respectively. It can be seen that at $P =$ 0GPa, the total DOS is dominated by the s states, reaching 100% at -5 eV, and the s states contribution gradually goes to zero as one approaches Fermi energy. At the same time, the d-state contribution gradually grows until it reaches a value of the order of 80% at E_F. Conversely, at high pressure, the s-state contribution remains approximately constant and small (below 20%), while the d-state contribution, starting at 100% at -5 eV, decreases slightly, but remains higher than 60% until few eV above Fermi energy. Thus, in our calculations, the $s \rightarrow d$ charge transfer appears more like a d bandwidth increase rather than a real transfer of the charge between the orbitals, which is ill-defined in a metallic system.

V. CONCLUSIONS

The structure of Y metal above 100 GPa, and thus the likely structure of the superconducting phase, is found to be face-centered orthorhombic ($oF16$), isostructural with that observed in the collapsed phases of the trivalent lanthanides Tb, Gd, Dy, Ho, Er, and (probably) Tm. This result confirms the close structural relationship between the lanthanides and yttrium, which has no f electrons. High-precision measurements of the compressibility reveal anomalous values at lower pressures, very similar to those seen in Sm, but that the compressibility of the $oF16$ phase is that of a regular metal, such as Au, Pt, or Cu. DFT calculations confirm the lower enthalpy of the $oF16$ structure relative to that of $oF8$ structure seen in Sm and Nd, and reveal that the $s \rightarrow d$ charge transfer occurs via a d-bandwidth increase, which enhances the relative contribution of the d-states to the density of states near the Fermi level.

Note added in proof. Buhot *et al.* [49] have recently reanalyzed the x-ray diffraction data of Samudrala *et al.* [13] at 123 GPa using Rietveld methods and shown that it can be fitted with the $oF16$ structure, while their superconductivity measurements show that the $oF16$ phase can be stabilized without partially occupied f states.

ACKNOWLEDGMENTS

British Crown Owned Copyright 2020/AWE. Published with permission of the Controller of Her Britannic Majesty's Stationery Office. This work was supported by grants (Grants No. EP/R02927X/1 and No. EP/R02992X/1) from the U.K. Engineering and Physical Sciences Research Council (EPSRC) and experimental facilities made available by DESY (Hamburg, Germany), a member of the Helmholtz Association HGF, and by the Diamond Light Source (DLS). The research leading to this result has been supported by the project CALIPSO plus under the Grant Agreement 730872 from the EU Framework Programme for Research and Innovation HORIZON 2020. We would like to thank R. J. Husband for her assistance on beamline P02.2 at PETRA III and D. Daisenberger for his support on the I15 beamline at DLS. S.E.F. and C.V.S. are grateful to AWE for the award of CASE studentships.

[1] U. Benedict, W. A. Grosshans, and W. B. Holzapfel, Physica B+C **144**, 14 (1986).
[2] T. Krüger, B. Merkau, W. A. Grosshans, and W. B. Holzapfel, High Pressure Res. **2**, 193 (1990).
[3] W. B. Holzapfel, Physica B **190**, 21 (1993).
[4] W. B. Holzapfel, J. Alloys Compd. **223**, 170 (1995).
[5] B. Johansson, Hyper. Interact. **128**, 41 (2000).
[6] G. K. Samudrala and Y. K. Vohra, in *Handbook on the Physics and Chemistry of Rare Earths* (Elsevier, Amsterdam, The Netherlands, 2013), Vol. 43, pp. 275–319.
[7] M. I. McMahon, S. Finnegan, R. J. Husband, K. A. Munro, E. Plekhanov, N. Bonini, C. Weber, M. Hanfland, U. Schwarz, and S. G. Macleod, Phys. Rev. B **100**, 024107 (2019).
[8] B. Johansson and A. Rosengren, Phys. Rev. B **11**, 2836 (1975).

[9] J. C. Duthie and D. G. Pettifor, Phys. Rev. Lett. **38**, 564 (1977).
[10] Y. K. Vohra, H. Olijnik, W. Grosshans, and W. B. Holzapfel, Phys. Rev. Lett. **47**, 1065 (1981).
[11] W. Grosshans, Y. Vohra, and W. Holzapfel, J. Magn. Magn. Mater. **29**, 282 (1982).
[12] Y. Chen, Q.-M. Hu, and R. Yang, Phys. Rev. B **84**, 132101 (2011).
[13] G. K. Samudrala, G. M. Tsoi, and Y. K. Vohra, J. Phys.: Condens. Matter **24**, 362201 (2012).
[14] W. H. Zachariasen, Proc. Natl. Acad. Sci. USA **75**, 1066 (1978).
[15] M. I. McMahon and R. J. Nelmes, Phys. Rev. Lett. **78**, 3884 (1997).
[16] S. E. Finnegan, E. J. Pace, C. V. Storm, M. I. McMahon, S. G. MacLeod, H.-P. Liermann, and K. Glazyrin, Phys. Rev. B **101**, 174109 (2020).
[17] S. Heathman, R. G. Haire, T. Le Bihan, A. Lindbaum, K. Litfin, Y. Méresse, and H. Libotte, Phys. Rev. Lett. **85**, 2961 (2000).
[18] S. Heathman, R. G. Haire, T. Le Bihan, A. Lindbaum, M. Idiri, P. Normile, S. Li, R. Ahuja, B. Johansson, and G. H. Lander, Science **309**, 110 (2005).
[19] S. Heathman, T. Le Bihan, S. Yagoubi, B. Johansson, and R. Ahuja, Phys. Rev. B **87**, 214111 (2013).
[20] Y. C. Zhao, F. Porsch, and W. B. Holzapfel, Phys. Rev. B **50**, 6603 (1994).
[21] G. N. Chesnut and Y. K. Vohra, Phys. Rev. Lett. **82**, 1712 (1999).
[22] C. S. Perreault and Y. K. Vohra, High Pressure Res. **40**, 392 (2020).
[23] Y. Chen, Q.-M. Hu, and R. Yang, Phys. Rev. Lett. **109**, 157004 (2012).
[24] P. Li, T. Mei, Z. Lu, L. Xiang, X. Zhang, X. Du, J. Wang, and H. Chen, Comput. Mater. Sci. **159**, 428 (2019).
[25] J. J. Hamlin, V. G. Tissen, and J. S. Schilling, Physica C **451**, 82 (2007).
[26] A. P. Durajski, Phys. Status Solidi B **252**, 2167 (2015).
[27] Y. Akahama, H. Fujihisa, and H. Kawamura, Phys. Rev. Lett. **94**, 195503 (2005).
[28] H. Nozomu, Y. Sakamoto, H. Fujihisa, Y. Fujii, K. Takemura, T. Kikegawa, and O. Shimomura, J. Phys.: Condens. Matter **5**, L369 (1993).
[29] N. Hamaya, N. Okabe, M. Yamakata, T. Yagi, and O. Shimomura, High Pressure Res. **14**, 287 (1996).
[30] Y. R. Shen, R. S. Kumar, A. L. Cornelius, and M. F. Nicol, Phys. Rev. B **75**, 064109 (2007).
[31] T. Ishikawa, T. Oda, N. Suzuki, and K. Shimizu, High Pressure Res. **35**, 37 (2015).
[32] T. S. Sokolova, P. I. Dorogokupets, A. M. Dymshits, B. S. Danilov, and K. D. Litasov, Comput. Geosci-UK **94**, 162 (2016).
[33] H. K. Mao, J. Xu, and P. M. Bell, J. Geophys. Res. **91**, 4673 (1986).
[34] A. Dewaele, M. Torrent, P. Loubeyre, and M. Mezouar, Phys. Rev. B **78**, 104102 (2008).
[35] C. Prescher and V. B. Prakapenka, High Pressure Res. **35**, 223 (2015).
[36] V. Petříček, M. Dušek, and L. Palatinus, Z. Krist-Cryst. Mater. **229**, 345 (2014).
[37] J. Rodríguez-Carvajal, Physica B **192**, 55 (1993).
[38] T. J. B. Holland and S. A. T. Redfern, Mineral. Mag. **61**, 65 (1997).
[39] S. R. Evans, I. Loa, L. F. Lundegaard, and M. I. McMahon, Phys. Rev. B **80**, 134105 (2009).
[40] R. J. Husband, I. Loa, K. Munro, and M. I. McMahon, J. Phys.: Conf. Ser. **500**, 032009 (2014).
[41] F. Porsch and W. B. Holzapfel, Phys. Rev. B **50**, 16212 (1994).
[42] A. Dewaele, P. Loubeyre, and M. Mezouar, Phys. Rev. B **70**, 094112 (2004).
[43] W. B. Holzapfel, High Pressure Res. **16**, 81 (1998).
[44] W. B. Holzapfel, Z. Krist-Cryst. Mater. **216**, 473 (2001).
[45] U. Herath, P. Tavadze, X. He, E. Bousquet, S. Singh, F. Muñoz, and A. H. Romero, Comput. Phys. Commun. **251**, 107080 (2020).
[46] G. Kresse and D. Joubert, Phys. Rev. B **59**, 1758 (1999).
[47] J. P. Perdew, K. Burke, and M. Ernzerhof, Phys. Rev. Lett. **77**, 3865 (1996).
[48] D. D. Koelling and B. N. Harmon, J. Phys. C: Solid State Phys. **10**, 3107 (1977).
[49] J. Buhot, O. Moulding, T. Muramatsu, I. Osmond, and S. Friedemann, Phys. Rev. B **102**, 104508 (2020).